Check for updates

Formation and functionalization of membraneless compartments in *Escherichia coli*

Shao-Peng Wei[1,3], Zhi-Gang Qian [ID][1,3], Chun-Fei Hu[1,3], Fang Pan[1], Meng-Ting Chen[1], Sang Yup Lee [ID][2] and Xiao-Xia Xia [ID][1✉]

Membraneless organelles formed by liquid–liquid phase separation of proteins or nucleic acids are involved in diverse biological processes in eukaryotes. However, such cellular compartments have yet to be discovered or created synthetically in prokaryotes. Here, we report the formation of liquid protein condensates inside the cells of prokaryotic *Escherichia coli* upon heterologous overexpression of intrinsically disordered proteins such as spider silk and resilin. In vitro reconstitution under conditions that mimic intracellular physiologically crowding environments of *E. coli* revealed that the condensates are formed via liquid–liquid phase separation. We also show functionalization of these condensates via targeted colocalization of cargo proteins to create functional membraneless compartments able to fluoresce and to catalyze biochemical reactions. The ability to form and functionalize membraneless compartments may serve as a versatile tool to develop artificial organelles with on-demand functions in prokaryotes for applications in synthetic biology.

Compartmentalization is commonly used by cells for spatially controlling their cellular materials, signaling and metabolic processes[1–3]. Examples of compartments in nature range from phospholipid membrane-bound organelles in eukaryotes[1] to protein-shelled microcompartments in prokaryotes[2]. Membraneless organelles, a newly defined type of cellular compartment, are reported to form via liquid–liquid phase separation (LLPS) within eukaryotic cells[3,4], but remain to be discovered in prokaryotes. These organelles, which are reversibly formed by concentrating proteins or nucleic acids[5,6], play crucial roles in cell physiology and pathology through their organization of the intracellular space[7].

Much effort has been exerted over the years to reprogram naturally occurring compartments or construct artificial organelles de novo for synthetic applications[8–10]. Membraneless organelles are of particular interest due to their intrinsic liquid-like properties that allow organelle components to freely exchange materials with the surrounding milieu. Furthermore, in many cases the formation of membraneless organelles can be driven by a single protein constituent[11–14], in contrast to the complex membrane-bound organelles which typically involve a large number of different biomacromolecules[1]. Due to their distinct structures and dynamic characteristics, some artificial membraneless organelles have been successfully reproduced in eukaryotes[13,15]. However, the ability to assemble them in prokaryotes is yet to be achieved due to the inherent aggregation-prone characteristics of LLPS proteins and the different cellular environments between prokaryotes and eukaryotes[3,16].

Here, we report the creation of artificial membraneless compartments with functionality in the model prokaryotic bacterium *E. coli*. We are inspired by the common features of eukaryotic LLPS proteins, typically comprising intrinsically disordered regions with low-complexity sequences, which are characterized by long stretches with a low overall diversity of amino acids rich in alanine, glycine and serine residues[3]. As these features were also observed in other natively unfolded, structural proteins such as spider silk[17,18] and resilin[19–21], we explore whether the formation of membraneless organelles could occur via LLPS of these proteins within *E. coli* cells. Cell imaging analyses revealed formation of the protein compartments in the poles of recombinant *E. coli* cells, with minimal effects on cell morphology. Intracellular compartmentalization of the proteins into soluble condensates was then reconstituted in vitro. Moreover, we demonstrate functionalization of the membraneless compartments via targeted colocalization of cargo proteins.

Results

Formation of silk protein compartments in *E. coli* cells. We first designed a recombinant major ampullate spidroin 1 (I16) of the spider *Nephila clavipes*, and fused it N-terminally to a green fluorescent protein (GFP) with a flexible linker to visualize its expression in *E. coli*. Confocal imaging revealed expression of the silk I16–GFP fusion as fluorescent condensates spatially localized near the pole regions of cells (Fig. 1a), while GFP alone produced fluorescence dispersed through the cytosol. The compartmentalized condensates of I16–GFP were liquid-like, given the fact that the fusion protein was expressed mainly in a soluble form rather than insoluble inclusion bodies (Supplementary Fig. 1). In addition, formation of the cellular compartments occurred under diverse experimental conditions, and was adjustable by varying the length of recombinant spidroins (Extended Data Fig. 1), and by modulating the temperature at which protein production was induced and the duration of postinduction (Extended Data Fig. 2). Notably, the cellular compartments formed were dynamic and could be disassembled by treating the compartmented cells with urea (Extended Data Fig. 3), further supporting that the condensates are liquid-like.

We next tested whether expression of spider silk I16 alone could form liquid protein condensates. As expected, a clear compartmentalization in the cells was observed by optical microscopy (Fig. 1b

[1]State Key Laboratory of Microbial Metabolism, Joint International Research Laboratory of Metabolic & Developmental Sciences, and School of Life Sciences and Biotechnology, Shanghai Jiao Tong University, Shanghai, People's Republic of China. [2]Metabolic and Biomolecular Engineering National Research Laboratory, Department of Chemical and Biomolecular Engineering (BK21 Plus Program), BioProcess Engineering Research Center, Bioinformatics Research Center, and Institute for the BioCentury, KAIST, Yuseong-gu, Republic of Korea. [3]These authors contributed equally: Shao-Peng Wei, Zhi-Gang Qian, Chun-Fei Hu. ✉e-mail: xiaoxiaxia@sjtu.edu.cn
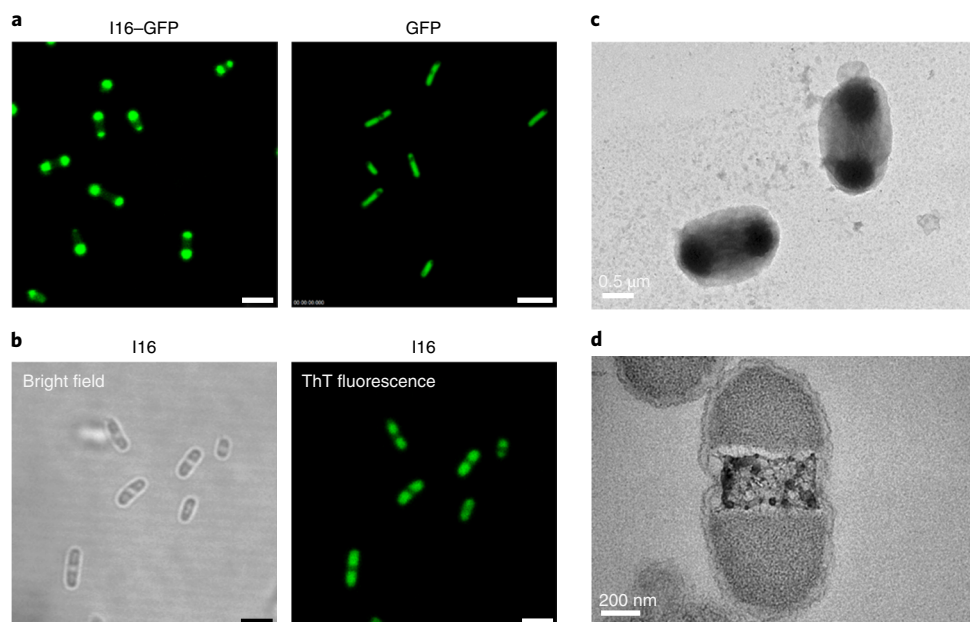
Fig. 1 | Formation of cellular compartments upon spider silk expression in *E. coli*. a, Fluorescence microscopy images of cells expressing GFP-tagged silk protein I16 (left panel). The right panel shows a uniform distribution of GFP except for the dark spot inside the cell, which corresponds to nonfluorescent inclusion bodies. Scale bar in left panel, 3 μm; scale bar in right panel, 5 μm. **b**, Bright-field and fluorescence microscopy images of I16-expressing cells stained with ThT, a fluorescent probe to detect β-sheet fibrillar structures. Scale bars, 3 μm. **c,d**, TEM images of fixed cells (**c**) and a fixed microtome slice (**d**) of a single cell expressing I16. All cells were cultivated at 37 °C and induced with 200 μM IPTG for gene expression. Cell samples were taken 6 h after induction. Data in **a**–**d** are representative of *n* = 3 independent experiments.

and Supplementary Fig. 2). Since β-sheet fibrils are prevalent in natural spider silk, it was hypothesized that such structures might also exist in the silk I16 condensates in vivo. To test this, a fluorescent dye that probes the β-sheet-rich structures[22], Thioflavin T (ThT), was used to stain the I16-expressing cells. Confocal images showed compartmentalized fluorescence that overlapped with the silk protein condensates (Fig. 1b), indicating that the condensates were rich in β-sheet content and permeable to the small-molecule dye. Such β-sheet structures did not lead to the aggregation of silk proteins into inclusion bodies (Supplementary Fig. 3). Instead, they might promote the formation of compartmentalized silk condensates via inter-chain interactions of the β-sheets. Transmission electron microscopy (TEM) of the I16-expressing cells further supported the formation of silk-based liquid compartments in the cytoplasm (Fig. 1c,d and Extended Data Fig. 4). Notably, the cell length and width were not substantially altered upon I16 expression, whereas the cell growth was moderately reduced (Extended Data Fig. 5).

Reconstitution of protein compartmentalization in vitro. Having established cellular membraneless compartments in live cells, we next performed in vitro reconstitution assays to explore the mechanism of silk protein compartmentalization in vivo. To this end, silk I16–GFP fusion protein was purified (Supplementary Fig. 4), and reconstituted into a buffer supplemented with dextran-70, a volume-excluding polymer frequently used to mimic intracellular physiological crowding environments[23]. The I16–GFP solution became turbid immediately upon mixing with dextran-70, which arose from micrometer-sized droplets in the reconstituted mixtures that are clearly visible by fluorescence and light microscopy (Fig. 2a and Extended Data Fig. 6a). The spherical droplets tended to fuse into larger ones (Fig. 2b and Supplementary Video 1). Upon centrifugation, the turbid mixture was separated into a more-fluorescent dense phase and a less-fluorescent light phase (Fig. 2a). Upon photobleaching of a single droplet, the majority of its fluorescence (~70%) was recovered with a characteristic recovery time of approximately

20.8 s (Fig. 2c). This indicated that the protein droplets were highly dynamic, with rapid exchange of molecules between the droplets and the surrounding solution. Notably, LLPS of the untagged I16 protein was also observed to occur at protein concentrations beyond certain critical levels and in the presence of an alternative macromolecular crowder (Extended Data Fig. 7). In addition, the LLPS facilitated the formation of β-sheets in the silk protein (Supplementary Fig. 5), and the phase separation was reversible upon dilution (Extended Data Fig. 8). These in vitro experiments reflected the liquid properties of the droplets and supported that the protein condensates were formed via LLPS of the spider silk protein.

Based on the above observations on compartmentalization in vitro and in vivo, we propose a model for the formation of compartmentalized spider silk condensates in *E. coli*. The newborn polypeptide chains of spider silk concentrated near ribosomes facilitate the inter-chain interaction and subsequently trigger the LLPS of silk proteins into liquid droplets and condensates. The high concentration of spider silk proteins within these condensates would facilitate hydrophobic interactions among poly-A stretches[17,24] present in the protein, and thus accelerate the formation of short β-sheets to stabilize the resulting membraneless compartments (Supplementary Fig. 6). These phase-separated spider silk proteins within *E. coli* might resemble the highly concentrated, aqueous spidroin proteins within the silk glands ready for spinning into solid silk fibers[17,24].

Compartments formed by other disordered proteins. We also explored whether cellular compartments could be formed by other intrinsically disordered structural proteins. Two other disordered proteins of low complexity, major ampullate spidroin 2 (termed II16; ref. [25]) and resilin-like protein (termed R32; ref. [21]), were tested for their ability to form membraneless compartments via LLPS. Interestingly, both II16 and R32 proteins could also form liquid droplets under crowded conditions in vitro (Extended Data Fig. 6b). In addition, both of them were able to form cellular compartments in the cytoplasm of *E. coli* cells (Extended Data Fig. 9). These results suggest
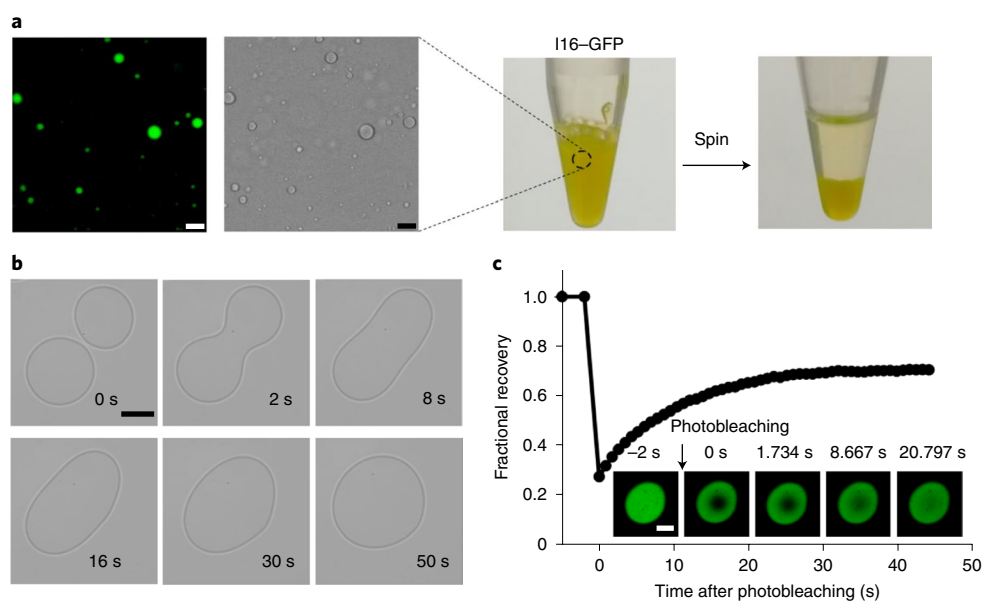
Fig. 2 | Formation of cellular compartments via LLPS. a, In vitro reconstitution of purified GFP-tagged I16 when mixed with the macromolecular crowding agent dextran-70. The turbid mixtures (middle panel) were visualized by fluorescence and bright-field light microscopy to reveal spherical droplets (left panel), and spun by centrifugation to show separation into two liquid phases (right panel). **b**, Light microscopy images showing time-lapse fusion of two individual liquid droplets. **c**, Representative fluorescence recovery of a partially photobleached droplet. The inset shows images of photobleaching on the droplet. Scale bars in **a**–**c**, 10 μm. Data in **a**–**c** are representative of $n = 3$ independent experiments.

the versatility of disordered structural proteins as building blocks for constructing intracellular membraneless compartments in *E. coli*.

Functionalization of synthetic cellular compartments. We next explored whether the cellular membraneless compartments could be targeted for colocalization of cargo proteins. As a model cargo, red fluorescent protein (RFP) was selected, which upon expression is normally distributed all over the cytoplasm. Three additional constructs were made, each encoding a carboxyl-terminal fusion of RFP to one of the structural proteins that themselves form cellular compartments (I16–RFP, II16–RFP and R32–RFP). The recombinant *E. coli* cells coexpressing I16–GFP and one of the RFP fusions were then examined by fluorescence microscopy. All of the RFP fusions formed fluorescent condensates near the pole regions of the cells, and more interestingly colocalized with the I16–GFP condensates, whereas RFP alone did not (Fig. 3a). These results suggest colocalization of diverse cargo proteins and the heterotypic interactions between structural proteins to form complex membraneless compartments within living cells.

Furthermore, we tested whether the synthetic membraneless compartments could be employed as nano-reactors for biocatalytic processes. As a proof-of-concept example, metallothionein (MT) was chosen as a catalytic cargo, which is rich in cysteine residues, binds heavy metals through clusters of thiolate bonds and reduces metal ions for the formation of functional metal nanoparticles[26]. For spatial localization at the membraneless compartments, a plasmid containing the gene encoding a spider silk I16–MT fusion protein was constructed for expression in *E. coli*. When these recombinant cells were incubated in a medium containing sodium selenite, homogenous Se nanoparticles with an average diameter of approximately 20 nm were formed and well dispersed in the compartments (Fig. 3b and Extended Data Fig. 10). This observation indicates that the free selenite ions can enter *E. coli* cells and then be reduced by the I16–MT condensates in the compartmentalized nano-reactors. In addition, these membraneless compartments seem to stabilize the newborn nanoparticles to prevent further aggregation and diffusion out of the compartments. In contrast, rather inhomogenous

nanoparticles were observed outside the cells of the control strain without I16–MT (Supplementary Fig. 7).

Finally, we examined whether the synthetic compartments could be equipped with multiple enzymes of a metabolic pathway for de novo biosynthesis of a specific chemical of interest in *E. coli*. To test this, the spider silk protein I16 was fused with both L-2,4-diaminobutyrate:α-ketoglutarate 4-aminotransferase (Dat) and L-2,4-diaminobutyrate decarboxylase (Ddc), which are responsible for the conversion of aspartate β-semialdehyde into 1,3-diaminopropane (1,3-DAP; Fig. 4a), a platform three-carbon diamine that finds wide applications in chemical industry[27]. As expected, coexpression of the fusion genes encoding the two enzymes resulted in a recombinant *E. coli* strain with the emergence of subcellular compartments (Fig. 4b,c). Specific production of 1,3-DAP on the basis of cell density (optical density at 600 nm (OD_{600})) was then determined. As shown in Fig. 4d, production of 1,3-DAP was slightly higher from the strain with fusion enzymes induced with 200 μM isopropyl-β-D-thiogalactoside (IPTG) than from the control strain with free enzymes ($t = 12$ h postinduction). Since the slight increase was not statistically significant (P value 0.08, analysis of variance (ANOVA)), the functionalized compartments with the two fusion enzymes did not show superior performance over free enzymes, which is contrary to expectation. One explanation for this could be that the architectural silk protein–enzyme fusions are more difficult than free enzymes to be biosynthesized de novo within the living cells of *E. coli*. Nonetheless, these experiments highlight the possibility of biofunctionalizing the membraneless compartments as a compartmentalized bioreactor capable of performing a cascade of reactions for metabolic engineering applications. To explore further potential of these synthetic compartments, studies are underway on colocalization of enzymes that are toxic to the bacterial host and catalyze reactions involving toxic metabolic intermediates.

Discussion

Our study demonstrates synthetic formation of a type of subcellular membraneless compartment in *E. coli*. These intracellular compartments are unique in that they are membraneless, form
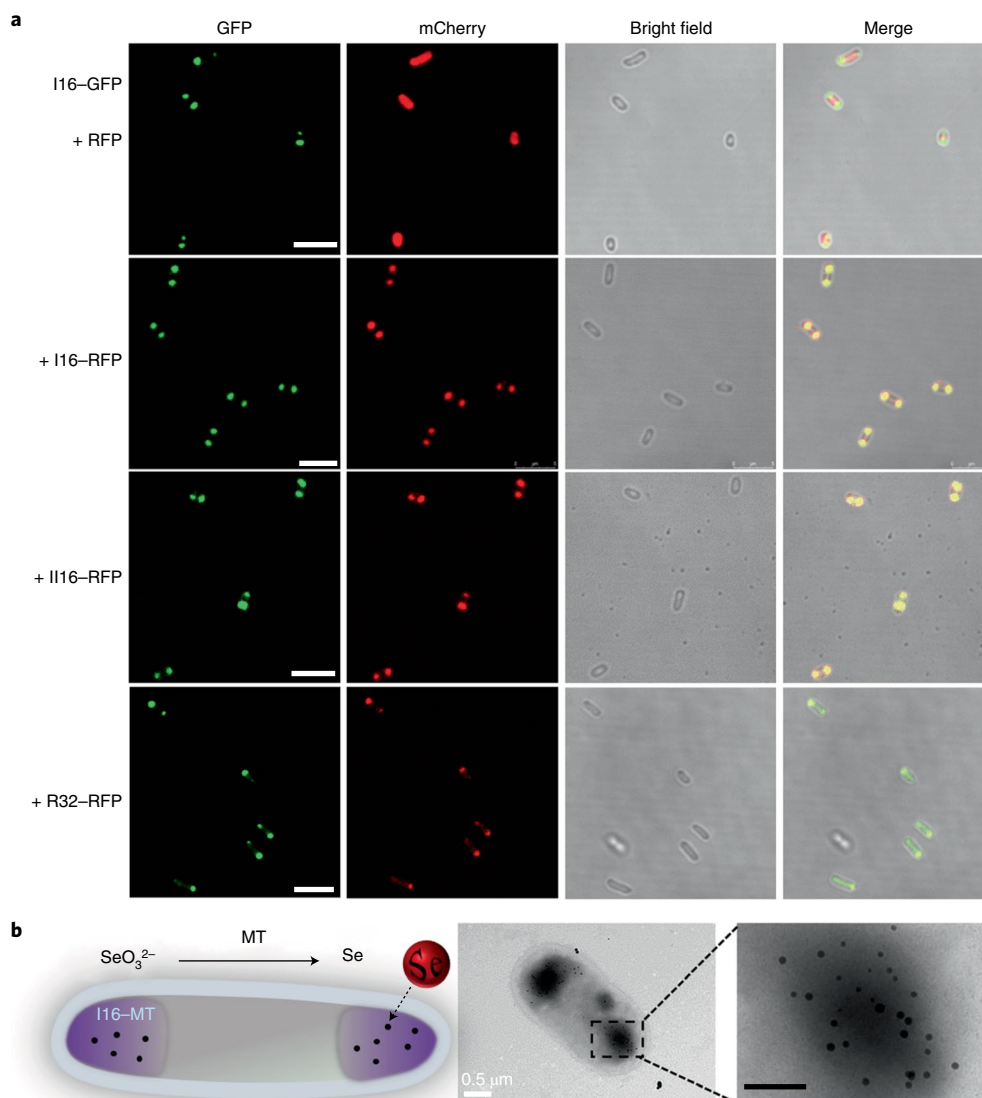
Fig. 3 | Functionalization of cellular compartments via targeted colocalization of cargo proteins. a, Colocalization of multiple fluorescent proteins in compartments upon coexpression of I16–GFP and RFP fused to I16, II16 and R32. Coexpression of I16–GFP and untagged RFP serves as a control. Scale bars, 5 μm. **b**, A schematic illustration of functionalizing cellular compartments by targeted localization of MT, a cargo protein that catalyzes the reduction of selenite into selenium (left panel). The middle panel shows a TEM image of a representative *E. coli* cell expressing silk protein I16 tagged with MT. Scale bar, 0.5 μm. The dotted-box area is zoomed in at the right panel (scale bar, 200 nm), showing the production of Se nanoparticles within the targeted compartments. Data in **a** and **b** are representative of *n* = 3 independent experiments.

through protein LLPS and exhibit liquid-like properties, which make them different from inclusion bodies and protein-shelled bacterial microcompartments. In addition, formation of these unique compartments can be driven by LLPS of a set of disordered structural proteins through homotypic interactions or heterotypic interactions if more than one structural protein exists. This inspired us to use these structural proteins as building blocks to construct complex functional compartments by directed colocalization of cargo proteins of interest, including two model fluorescent proteins, an enzyme forming metal nanoparticles and enzymes catalyzing two sequential biochemical reactions. Further on-demand control over assembly and disassembly of these compartments may be implemented with the tools previously developed for dynamic control of cellular compartments in eukaryotes[15,28,29].

Our subcellular compartments are speculated to evolve from de novo biosynthesized proteins via interactions of intrinsically disordered macromolecular chains in the crowded intracellular environment, in contrast with inclusion bodies that mainly result from misfolding and aggregation of proteins with intrinsic folding characteristics[30,31]. Here, we summarize four lines of evidence as to the clear distinction of our compartments from inclusion bodies. First, the silk proteins themselves and in fusion with GFP were found in the soluble fraction of the recombinant cells (Supplementary Figs. 1 and 3). Second, our protein condensates were as active as their soluble counterparts (Extended Data Fig. 2), in contrast with the proteins in inclusion bodies that are inactive, and those in active inclusion bodies having low levels (1–18%) of activity[32]. Third, the cellular condensates are readily disassembled by exposing the cells to 0.5–1 M urea for only 20 min, while largely retaining their fluorescence (Extended Data Fig. 3). Were the compartments inclusion bodies, a much higher concentration of urea (usually 6–8 M) would have been required to disrupt the cells and solubilize the inclusion bodies, which would have inactivated their fluorescence. Therefore, the cellular condensates are liquid-like. Finally, the purified proteins
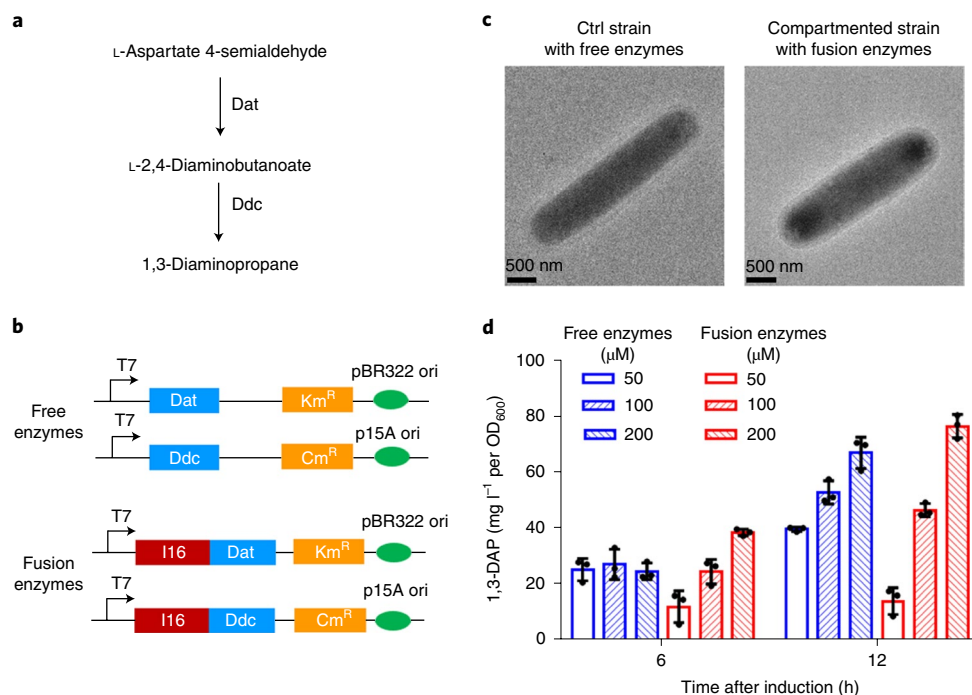
Fig. 4 | Functionalized intracellular compartments catalyze a cascade of two reactions. a, Schematic illustration of a cascade of reactions catalyzed by Dat and Ddc from the bacterium *A. baumannii* ATCC 19606. The cascade converts L-aspartate 4-semialdehyde, an endogenous metabolic intermediate of *E. coli*, into 1,3-DAP. **b**, Illustration of genetic constructs for overexpression of free enzymes Dat and Ddc or fusions at the carboxy-terminus of spider silk protein I16. **c**, TEM images of *E. coli* BL21(DE3) cells coexpressing free enzymes (Ctrl strain) or fusion enzymes (Compartmented strain). The cell samples were taken at 6 h postinduction with 100 μM IPTG at 30 °C. **d**, Specific production of 1,3-DAP in the culture media of recombinant strains induced with varying levels of IPTG. Data are presented as mean ± s.d. of $n = 3$ biologically independent samples, with individual data points shown as black dots. Statistical significance was determined using one-way ANOVA for *P* values. Data in **c** and **d** are representative of $n = 2$ independent experiments. Cm[R], chloramphenicol resistance gene; Km[R], kanamycin resistance gene; ori, origin of replication; T7, T7 promoter.

from the cellular compartments were soluble and homogeneous in hydrodynamic size, and existed mainly as single protein chains (Supplementary Fig. 4), and such a 'unimer' state ruled out the tentative disintegration of active inclusion body particles due to cell lysis and dilution.

Orthogonality is a desirable property in synthetic biology that has been difficult to achieve in constructing artificial, intracellular devices without harming the cell[33,34]. To examine orthogonality of the synthetic compartments to the host cell, we tested whether formation of the compartments upon overexpression of silk or resilin protein affected the normal cell physiology. The results showed that overexpression of these proteins did not substantially alter cell morphology, whereas approximately 20% reduction in the final cell biomass was observed when compared with the control (Extended Data Fig. 5). It is well recognized that recombinant protein production competes for cellular resources of the host, and thus inevitably leads to a certain degree of reduction in cell growth[35,36]. Therefore, the 20% reduction in growth of the compartmented cells is reasoned moderate and acceptable for general biotechnological applications.

Taken together, this study not only offers a compartmentalization strategy in *E. coli*, but also opens the door to the exploration of natural membraneless compartments in prokaryotes. Similar approaches can be taken for establishing artificial membraneless organelles in other prokaryotic and eukaryotic organisms for applications in biocatalysis, metabolic engineering and synthetic biology.

Online content
Any methods, additional references, Nature Research reporting summaries, source data, extended data, supplementary information, acknowledgements, peer review information; details of author contributions and competing interests; and statements of data and code availability are available at https://doi.org/10.1038/s41589-020-0579-9.

References
1. Hammer, S. K. & Avalos, J. L. Harnessing yeast organelles for metabolic engineering. *Nat. Chem. Biol.* **13**, 823–832 (2017).
2. Kerfeld, C. A., Aussignargues, C., Zarzycki, J., Cai, F. & Sutter, M. Bacterial microcompartments. *Nat. Rev. Microbiol.* **16**, 277–290 (2018).
3. Alberti, S., Gladfelter, A. & Mittag, T. Considerations and challenges in studying liquid–liquid phase separation and biomolecular condensates. *Cell* **176**, 419–434 (2019).
4. Boeynaems, S. et al. Protein phase separation: a new phase in cell biology. *Trends Cell Biol.* **28**, 420–435 (2018).
5. Saito, M. et al. Acetylation of intrinsically disordered regions regulates phase separation. *Nat. Chem. Biol.* **15**, 51–61 (2019).
6. Aumiller, W. M. Jr & Keating, C. D. Phosphorylation-mediated RNA/peptide complex coacervation as a model for intracellular liquid organelles. *Nat. Chem.* **8**, 129–137 (2016).
7. Shin, Y. & Brangwynne, C. P. Liquid phase condensation in cell physiology and disease. *Science* **357**, eaaf4382 (2017).
8. Lee, M. J. et al. Engineered synthetic scaffolds for organizing proteins within the bacterial cytoplasm. *Nat. Chem. Biol.* **14**, 142–147 (2018).
9. Lau, Y. H., Giessen, T. W., Altenburg, W. J. & Silver, P. A. Prokaryotic nanocompartments form synthetic organelles in a eukaryote. *Nat. Commun.* **9**, 1311 (2018).
10. Huber, M. C. et al. Designer amphiphilic proteins as building blocks for the intracellular formation of organelle-like compartments. *Nat. Mater.* **14**, 125–132 (2015).
11. Wei, M. T. et al. Phase behaviour of disordered proteins underlying low density and high permeability of liquid organelles. *Nat. Chem.* **9**, 1118–1125 (2017).
12. Uversky, V. N. Intrinsically disordered proteins in overcrowded milieu: membrane-less organelles, phase separation, and intrinsic disorder. *Curr. Opin. Struct. Biol.* **44**, 18–30 (2017).

13. Reinkemeier, C. D., Girona, G. E. & Lemke, E. A. Designer membraneless organelles enable codon reassignment of selected mRNAs in eukaryotes. *Science* **363**, eaaw2644 (2019).

14. Banani, S. F., Lee, H. O., Hyman, A. A. & Rosen, M. K. Biomolecular condensates: organizers of cellular biochemistry. *Nat. Rev. Mol. Cell Biol.* **18**, 285–298 (2017).

15. Zhao, E. M. et al. Light-based control of metabolic flux through assembly of synthetic organelles. *Nat. Chem. Biol.* **15**, 589–597 (2019).

16. Alberti, S. et al. A user's guide for phase separation assays with purified proteins. *J. Mol. Biol.* **430**, 4806–4820 (2018).

17. Heim, M., Keerl, D. & Scheibel, T. Spider silk: from soluble protein to extraordinary fiber. *Angew. Chem. Int. Ed. Engl.* **48**, 3584–3596 (2009).

18. Xia, X. X. et al. Native-sized recombinant spider silk protein produced in metabolically engineered *Escherichia coli* results in a strong fiber. *Proc. Natl Acad. Sci. USA* **107**, 14059–14063 (2010).

19. Lyons, R. E. et al. Comparisons of recombinant resilin-like proteins: repetitive domains are sufficient to confer resilin-like properties. *Biomacromolecules* **10**, 3009–3014 (2009).

20. Huang, S. C. et al. Rational design and hierarchical assembly of a genetically engineered resilin–silk copolymer results in stiff hydrogels. *ACS Biomater. Sci. Eng.* **3**, 1576–1585 (2017).

21. Hu, X., Xia, X. X., Huang, S. C. & Qian, Z. G. Development of adhesive and conductive resilin-based hydrogels for wearable sensors. *Biomacromolecules* **20**, 3283–3293 (2019).

22. Biancalana, M. & Koide, S. Molecular mechanism of Thioflavin-T binding to amyloid fibrils. *Biochim. Biophys. Acta* **1804**, 1405–1412 (2010).

23. Ellis, R. J. Macromolecular crowding: an important but neglected aspect of the intracellular environment. *Curr. Opin. Struct. Biol.* **11**, 114–119 (2001).

24. Oktaviani, N. A. et al. Conformation and dynamics of soluble repetitive domain elucidates the initial β-sheet formation of spider silk. *Nat. Commun.* **9**, 2121 (2018).

25. Yang, Y. X., Qian, Z. G., Zhong, J. J. & Xia, X. X. Hyper-production of large proteins of spider dragline silk MaSp2 by *Escherichia coli* via synthetic biology approach. *Process Biochem.* **51**, 484–490 (2016).

26. Choi, Y., Park, T. J., Lee, D. C. & Lee, S. Y. Recombinant *Escherichia coli* as a biofactory for various single- and multi-element nanomaterials. *Proc. Natl Acad. Sci. USA* **115**, 5944–5949 (2018).

27. Chae, T. U., Kim, W. J., Choi, S., Park, S. J. & Lee, S. Y. Metabolic engineering of *Escherichia coli* for the production of 1,3-diaminopropane, a three carbon diamine. *Sci. Rep.* **5**, 13040 (2015).

28. Nott, T. J. et al. Phase transition of a disordered nuage protein generates environmentally responsive membraneless organelles. *Mol. Cell* **57**, 936–947 (2015).

29. Schuster, B. S. et al. Controllable protein phase separation and modular recruitment to form responsive membraneless organelles. *Nat. Commun.* **9**, 2985 (2018).

30. Rinas, U. et al. Bacterial inclusion bodies: discovering their better half. *Trends Biochem. Sci.* **42**, 726–737 (2017).

31. Krauss, U., Jäger, V. D., Diener, M., Pohl, M. & Jaeger, K. E. Catalytically-active inclusion bodies—carrier-free protein immobilizates for application in biotechnology and biomedicine. *J. Biotechnol.* **258**, 136–147 (2017).

32. Jäger, V. D. et al. Tailoring the properties of (catalytically)-active inclusion bodies. *Microb. Cell Fact.* **18**, 33 (2019).

33. Meyer, A. J., Segall-Shapiro, T. H., Glassey, E., Zhang, J. & Voigt, C. A. *Escherichia coli* 'Marionette' strains with 12 highly optimized small-molecule sensors. *Nat. Chem. Biol.* **15**, 196–204 (2019).

34. Liu, C. C., Jewett, M. C., Chin, J. W. & Voigt, C. A. Toward an orthogonal central dogma. *Nat. Chem. Biol.* **14**, 103–106 (2018).

35. Scott, M., Gunderson, C. W., Mateescu, E. M., Zhang, Z. & Hwa, T. Interdependence of cell growth and gene expression: origins and consequences. *Science* **330**, 1099–1102 (2010).

36. Klumpp, S., Scott, M., Pedersen, S. & Hwa, T. Molecular crowding limits translation and cell growth. *Proc. Natl Acad. Sci. USA* **110**, 16754–16759 (2013).

Methods

Plasmid construction. All plasmids used in this study are listed in Supplementary Table 1, and the oligonucleotide primers used are listed in Supplementary Table 2. *E. coli* DH5α was routinely used for cloning and plasmid propagation, and grown in selective Luria–Bertani medium or on Luria–Bertani plates with 1.5 wt% agar. Antibiotics were added for selection at the following concentrations: 100 μg ml^{-1} ampicillin, 30 μg ml^{-1} chloramphenicol and 50 μg ml^{-1} kanamycin. The DNA sequences of the plasmid constructs containing PCR-amplified fragments were confirmed by sequencing. The amino acid sequences of the encoded proteins (spider silk protein I16, II16 and resilin R32) are listed in the Supplementary Note.

A tailor-made vector, pET28a4, was constructed for the expression of GFP fusions under the T7 promoter. First, plasmid pET28a(+) with a medium copy number (~30 copies per cell; Novagen) was subjected to site-directed mutagenesis to insert a *Bam*HI site downstream of the plasmid multiple cloning sites, using primers F28a4Ba and R28a4. Second, plasmid pET19b-MaSpI16 encoding 16 repeats of the consensus sequence of spider *N. clavipes* MaSp1 was generated by an iterative polymerization strategy on plasmid pET19b-MaSpI4 (ref. [25]). The 1.6-kilobase (kb), *Xho*I–*Nde*I silk fragment of pET19b-MaSpI16 was then subcloned into pET28a4, leading to pET28a4-MaSpI16. The 5.7-kb, *Spe*I–*Xma*I fragment of pET28a4-MaSpI16 was subsequently ligated with the 2.8-kb, *Nhe*I–*Xma*I fragment of pET28a4-MaSpI16 to construct plasmid pET28a4-MaSpI32. The DNA fragment encoding GFPmut3 (ref. [37]) was amplified from a laboratory stock plasmid pET19b-gfp′E16C with primers FgfpSpe and RgfpBam. The amplified fragment was digested with *Spe*I-HF and *Bam*HI-HF, and cloned into plasmid pET28a4-MaSpI16 at the same sites, resulting in plasmid pET28a4-I16-gfp′, which allows recombinant expression of I16 N-terminally fused to GFP with a flexible linker, (GGS)$_4$. This linker was also present in the protein fusions described in the following part of this section. The restricted fragment of *gfpmut3* was also cloned into plasmid pET28a4-MaSpI32 to make plasmid pET28a4-I32-gfp′. For the expression of I4 N-terminally fused to GFP, plasmid pET28a4-I4-gfp′ was constructed by ligating the 0.4-kb, *Spe*I–*Nde*I silk fragment of pET19b-MaSpI4 with the 6.0-kb, *Nde*I–*Spe*I fragment of pET28a4-I16-gfp′. For the expression of resilin N-terminally fused to GFP, plasmid pET19b-R32 encoding 32 repeats of the resilin-like consensus sequence[21] was digested with *Nde*I and *Spe*I-HF, and the resilin-like gene was inserted into pET28a4-I16-gfp′ at the same sites, resulting in pET28a4-R32-gfp′. Similarly, the DNA encoding 16 repeats of the consensus sequence of spider *N. clavipes* MaSp2 was liberated from plasmid pET28a-MaSpII16 (ref. [25]) and inserted into pET28a4-I16-gfp′ to yield pET28a4-II16-gfp′.

A series of expression vectors were also made for expression of RFP fusions. The DNA fragment encoding a monomeric RFP, mCherry, was amplified from a laboratory stock plasmid, pZA27mCherry, with primers FrfpSpe and RrfpBam. The amplified fragment was then digested with *Spe*I-HF and *Bam*HI-HF and cloned into plasmid pET28a4-MaSpI16 at the same sites, leading to plasmid pET28a4-I16-rfp. This plasmid was subsequently digested with *Nco*I-HF and *Bam*HI-HF to liberate the I16-rfp fragment for subcloning into a low-copy-number vector, pACYCDuet-1 (~15 copies per cell; Novagen), to make plasmid pACYC-I16-rfp. Plasmid pET28a-MaSpII16 was digested with *Nco*I-HF and *Spe*I-HF, and the resulting MaSp2 fragment was used to replace the MaSp1 fragment in pACYC-I16-rfp, leading to pACYC-II16-rfp. Similarly, pET19b-R32 was digested and the resilin-like fragment was used to construct pACYC-R32-rfp.

For cytoplasmic expression of fluorescent proteins as controls, plasmids pACYC-rfp and pET28a5-gfp′ were constructed. The DNA fragment encoding mCherry was amplified from template plasmid pET28a4-I16-rfp by PCR using primers FrfpNdeI and RrfpXhoI, digested with *Nde*I and *Xho*I, and inserted into vector pACYC-Duet1 at the same sites, resulting in plasmid pACYC-rfp. Before construction of pET28a5-gfp′, expression vector pET28a5 was made by site-directed mutagenesis of the *Nco*I site of pET28a4 into the *Kpn*I site using primers F28a5Kp and R28a5. The *gfpmut3* fragment was then amplified from template plasmid pET28a4-I16-gfp′ by PCR using primers FgfpKpn and RgfpBam2, digested with *Bam*HI-HF and *Kpn*I-HF, and cloned into pET28a5 to yield pET28a5-gfp′. For recombinant expression of hexahistidine-tagged GFP, the *gfpmut3* fragment was amplified from the template plasmid pET28a4-I16-gfp′ with primers F-GFPNde and R-GFPBam, digested with *Nde*I and *Bam*HI-HF, and inserted into pET28a4-I16-gfp′ at the same sites, leading to plasmid pET28a4-gfp′.

Plasmids were also constructed for the expression of spider silk–catalytic enzyme fusions. The DNA fragment encoding MT, corresponding to the PP_3262 gene of *Pseudomonas putida*, KT2440 (ref. [26]), was PCR amplified from the genomic DNA with primers FMTSpe and RMTBam, digested with *Spe*I-HF and *Bam*HI-HF, and ligated into plasmid pET28a4-MaSpI16 at the same sites, resulting in pET28a4-I16-MT. Similarly, the *ddc* gene encoding L-2,4-diaminobutanoate decarboxylase was amplified from the genomic DNA of *Acinetobacter baumannii* ATCC 19606 with primers FddcSpe and RddcBam, and cloned into pET28a4-MaSpI16 to construct plasmid pET28a4-I16-ddc. The *ddc* fragment was then subcloned into pACYC-I16-rfp at the *Spe*I and *Bam*HI sites to make plasmid pACYC-I16-ddc. The *dat* gene encoding 2-ketoglutarate 4-aminotransferase was also amplified from *A. baumannii* with primers FdatSpe and RdatBam, and then cloned into plasmid pACYC-I16-rfp to yield pACYC-I16-dat. The *dat* fragment

was subcloned into pET28a4-MaSpI16 at the *Spe*I and *Bam*HI sites to make plasmid pET28a4-I16-dat.

Plasmids were also made for individual expression of pathway enzymes without fusion. The *dat* gene was amplified from the genomic DNA of *A. baumannii* ATCC 19606 with primers FdatNdeI and RdatXhoI, cloned into the *Nde*I–*Xho*I site of pACYCDuet-1 (Novagen) to make pACYC-dat and then subcloned into pET28a4 at the same site to make plasmid pET28a4-dat. The *ddc* gene was amplified with primers F-ddcNde and R-ddcXho, digested with *Nde*I and *Xho*I, and then cloned into pACYC-dat to make pACYC-ddc.

Strains and culture condition. For protein expression and cell imaging studies, recombinant cells of *E. coli* BL21(DE3) harboring relevant plasmids were cultivated at 37 °C in a 250-ml flask containing 20 ml of selective Luria–Bertani medium (per liter: 10 g of tryptone, 5 g of yeast extract and 10 g of NaCl) in a shaking incubator at 220 r.p.m. When the cell OD$_{600}$ reached ~0.6, cells were induced with 200 μM isopropyl-β-D-thiogalactoside (IPTG) at 16, 30 or 37 °C as noted. Samples were taken at 6 or 12 h after induction for SDS–PAGE, microscopy, TEM and fluorescence measurements. To biosynthesize Se nanoparticles, recombinant cells of *E. coli* BL21(DE3) harboring plasmid pET28a4-I16-MT were induced with 200 μM IPTG at 30 °C for 1 h before the addition of 5 mM sodium selenite. To biosynthesize 1,3-DAP, recombinant cells of *E. coli* BL21(DE3) cotransformed with pET28a4-I16-dat and pACYC-I16-ddc, and the control strain cotransformed with pET28a4-dat and pACYC-ddc, were grown at 37 °C in flasks containing 50 ml of R/2 medium supplemented with 10 g l^{-1} glucose and 3 g l^{-1} (NH$_4$)$_2$SO$_4$ (ref. [38]), and induced at 30 °C with varying levels of IPTG when OD$_{600}$ reached ~1.4. Samples were taken at the indicated time points for TEM analyses and quantification of 1,3-DAP.

SDS–PAGE and protein solubility analyses. Cells were collected by centrifugation at 10,000*g* for 10 min at 4 °C, and the resulting cell pellets were resuspended and lysed with One Step Bacterial Active Protein Extraction Kit (Sangon Biotech). The cell lysates were centrifuged to yield the supernatants (soluble fraction) and the pellets (precipitate fraction). The Laemmli sample buffer was then used to prepare the protein samples before separation on 10% SDS–PAGE gels. The gels were stained with Coomassie brilliant blue R250 (Bio-Rad), and scanned by using a Microtek Bio-5000 Plus scanner (Microtek).

Confocal imaging. The confocal images were collected on the Leica TCS SP8 STED 3X microscope (Leica Microsystems). Recombinant cells of *E. coli* expressing fluorescent proteins were collected by centrifugation, washed with PBS and then transferred (~10 μl) onto glass slides. For ThT staining of silk protein-expressing cells, the collected cells were suspended with 0.1 mg ml^{-1} ThT in PBS to an OD$_{600}$ value of approximately 1 for 10 min at room temperature. The stained cells were then washed twice with fresh PBS before being loaded onto the glass slides. The specimens were illuminated with a 488-nm laser for green fluorescence imaging and with a 561-nm laser for red fluorescence imaging. Images were processed and analyzed with the Leica Las X software (Leica Microsystems).

Cell fluorescence measurements. Fluorescence measurements were carried out on a Spark multimode microplate reader (Tecan). The cells expressing GFPmut3 were washed with PBS, resuspended and then loaded onto a 96-well cell culture plate (Nest Biotechnology) for measurement of fluorescence (excitation, 488 nm; emission, 507 nm).

TEM. TEM was conducted on a Tecnai G^2 Spirit BioTWIN transmission electron microscope (FEI Company) at an accelerating voltage of 120 kV. Images were recorded using a Gatan 832 CCD camera (Gatan). For direct TEM imaging, the cells were collected by centrifugation and washed with deionized water three times. Upon resuspension with water, 10 μl of the cell suspension was transferred onto a copper grid to let stand for 15 min. The excess liquid was blotted off on a filter paper, and the specimens were air dried and then examined in the microscope. For imaging of fixed slices of cells, the collected cells were suspended with 2.5% glutaraldehyde in PBS and incubated overnight at room temperature. The cells were subsequently washed with 0.1 M phosphate buffer (pH 7.4), and stained with 1% osmium tetroxide in the above phosphate buffer for 2 h. Upon dehydration in graded ethanol and acetone, the cells were embedded in epoxide resin and incubated at 55 °C for 2 d. The polymerized blocks were cut into slices with a thickness of 50 nm using a Leica EM UC7 microtome (Leica Microsystems). The slices were subsequently transferred onto the copper grids, stained with lead citrate and uranyl acetate, and then rinsed in deionized water. The specimens were then air dried for TEM imaging.

Protein purification. The collected cells were resuspended in 5 mM Tris-HCl buffer (pH 8.0) containing 150 mM NaCl and 5 mM imidazole, and then lysed using a high-pressure homogenizer. The supernatant of cell lysate was loaded onto a nickel-nitrilotriacetic acid (Ni-NTA) agarose resin column for affinity purification. The eluted proteins with 250 mM imidazole were dialyzed against 10 mM phosphate buffer (pH 7.4) supplemented with 200 mM NaCl. The purified

proteins were then concentrated using Amicon Ultra-15 centrifugal filter units with Ultracel-10K membranes (Millipore).

Dynamic light scattering. Dynamic light scattering was carried out on a NanoBrook Omni system (BrookHaven Instruments) equipped with a temperature controller. Each protein at 1 mg ml^{-1} was introduced into quartz cuvettes, and the samples were stabilized at 25 °C for 10 min before measurements. Number distribution data were collected from five measurements, and analyzed using the instrument built-in software (BrookHaven Instruments).

In vitro droplet formation and fluorescence assay. The concentrated solutions of each purified protein were mixed with an equal volume of 100 mg ml^{-1} dextran-70 (Sangon Biotech) in 10 mM phosphate buffer (pH 7.4) containing 200 mM NaCl with mild mixing. Alternatively, the purified proteins were mixed with an equal volume of 200 mg ml^{-1} Ficoll 70 (Sangon Biotech). The resulting turbid mixtures were then loaded onto glass slides and visualized by light and confocal fluorescence microscopy (Leica Microsystems). The fusion of individual droplets was monitored under an Olympus BX43 microscope (Olympus). The turbid mixtures were also centrifuged for separation into two coexisting liquid phases, and the lower liquid phase with enriched silk protein was stained with 50 μM ThT for fluorescence assay (excitation, 440 nm; emission, 488 nm).

Fluorescence recovery after photobleaching. Fluorescence recovery after photobleaching experiments were conducted under the Leica TCS SP8 STED 3X microscope (Leica Microsystems). The protein droplets formed with purified proteins and dextran-70 were loaded onto glass slides under the microscope. The droplets were activated at 488 nm with 5% laser power to show appropriate green light intensity, whereas photobleaching was initiated by irradiation with 100% laser power onto the droplet center with a radius of ~4 μm for 2 s. The fluorescence intensity within the selected region was monitored and normalized to the intensity before bleaching.

HPLC analysis. Upon centrifugation, the cell-free supernatants were filtered through a 0.22-μm membrane for quantification of 1,3-DAP levels. 1,3-DAP was precolumn derivatized with *o*-phthaldialdehyde (Sigma) and quantified by reverse-phase HPLC with ultraviolet detection at 230 nm as described in our previous study[38], except that 1,3-DAP (Tokyo Kasei Kogyo) was used as an authentic standard.

Statistical analysis. Information regarding error bars, number of biological replicates or samples, number of independent experiments and statistical analyses are described in the corresponding figures.

Reporting Summary. Further information on research design is available in the Nature Research Reporting Summary linked to this article.

Data availability

All data that support the findings of this study are available within the paper, the supplementary information and the source data or from the corresponding author upon reasonable request. Source data are provided with this paper.

References

37. Gardner, T. S., Cantor, C. R. & Collins, J. J. Construction of a genetic toggle switch in *Escherichia coli*. *Nature* **403**, 339–342 (2000).
38. Qian, Z. G., Xia, X. X. & Lee, S. Y. Metabolic engineering of *Escherichia coli* for the production of putrescine: a four carbon diamine. *Biotechnol. Bioeng.* **104**, 651–662 (2009).

Acknowledgements

Author contributions

X.-X.X., Z.-G.Q. and S.-P.W. conceived the project. Z.-G.Q. and X.-X.X. designed the research, analyzed the data and wrote the manuscript. S.-P.W. performed plasmid construction, cell imaging, droplets fusion and photobleaching experiments; analyzed the data; and wrote the draft. C.-F.H. performed recombinant protein production, purification and reconstitution experiments. F.P. constructed recombinant strains for 1,3-diaminopropane biosynthesis, performed urea perturbation experiments and aided plasmid construction. M.-T.C. performed 1,3-diaminopropane production experiments and aided plasmid construction. S.Y.L. analyzed the data and revised the manuscript.

Competing interests

X.-X.X., S.-P.W., M.-T.C., F.P. and Z.-G.Q. have filed a patent application ('Construction and applications of membraneless organelles in prokaryotic *Escherichia coli*', Chinese Patent Application No. 201910929503.X) on the basis of this contribution.
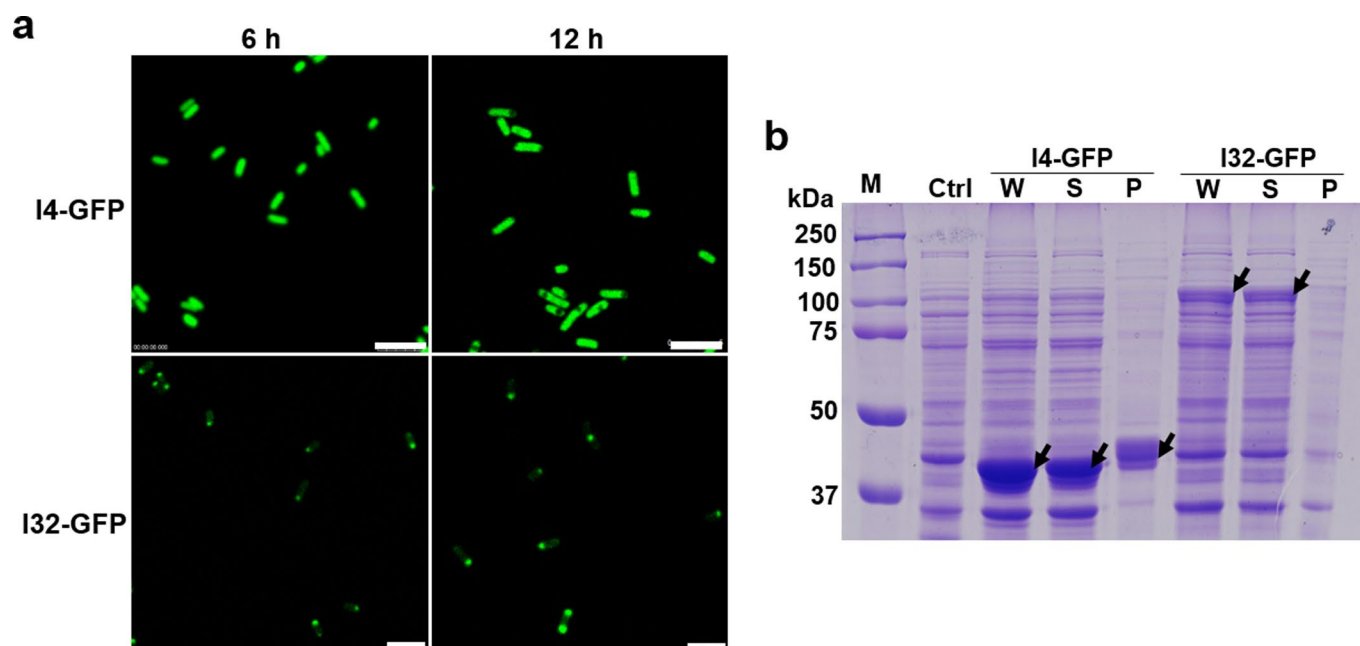
Additional information

**Extended data** is available for this paper at https://doi.org/10.1038/s41589-020-0579-9.

Supplementary information is available for this paper at https://doi.org/10.1038/s41589-020-0579-9.

Correspondence and requests for materials should be addressed to X.-X.X.

**Reprints and permissions information** is available at www.nature.com/reprints.

Extended Data Fig. 1 | Formation of compartments was adjustable by varying the spidroin length. a, Confocal images of *E. coli* cells expressing I4-GFP and I32-GFP. Cell samples were taken 6 or 12 h after induction at 30 °C for protein production. Scale bars, 5 μm. **b**, SDS-PAGE analysis of I4-GFP and I32-GFP expression. Lanes: M, molecular weight marker; W, whole cell extract; S, supernatant of whole cell extract; P, pellets of whole cell extract. The induced cells were taken at 6 h after exposure to the inducer IPTG for silk gene expression, and the uninduced cells were included as a control. The arrows indicate the respective target proteins, and uncropped gel is displayed in Source Data. Data in **a**, **b** are representative of *n* = 3 independent experiments.
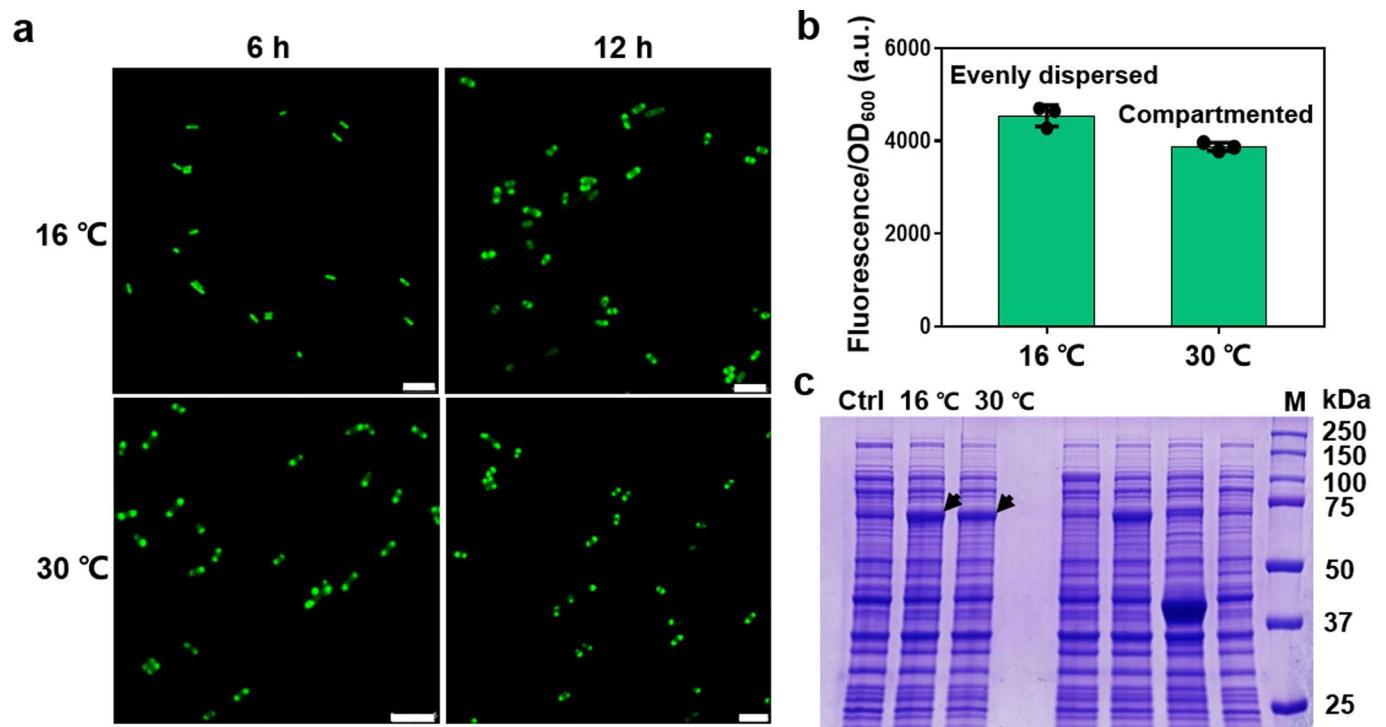
Extended Data Fig. 2 | Formation of compartments was adjustable by modulating the induction temperature and duration of post-induction. a, Confocal images of the cellular compartments in *E. coli* cells expressing silk I16-GFP at diverse temperatures. Cell samples were taken 6 or 12 h after inducing protein expression. Scale bar in the upper left panel, 8 μm; scale bars in the other panels, 5 μm. Note that clear compartmentalization was observed for the cells induced at 16 °C for 12 h, but not at 6 h. The condensates do not form as rapidly as at higher temperatures, which might be due to that lower temperature leads to the lower rate of protein expression. Data are representative of *n* = 3 independent experiments. **b**, Specific fluorescence per OD_{600} (arbitrary units, a.u.) of the cells with evenly dispersed or compartmented I16-GFP at the indicated induction temperature for 6 h. Data are presented as mean ± s.d. of *n* = 3 biologically independent samples, with individual data points shown as black dots. **c**, SDS-PAGE analysis of the cellular protein extracts from the cells described in **b**. The uninduced cells were included as a control, and uncropped gel is displayed in Source Data. Data in **b** and **c** are representative of *n* = 2 independent experiments.
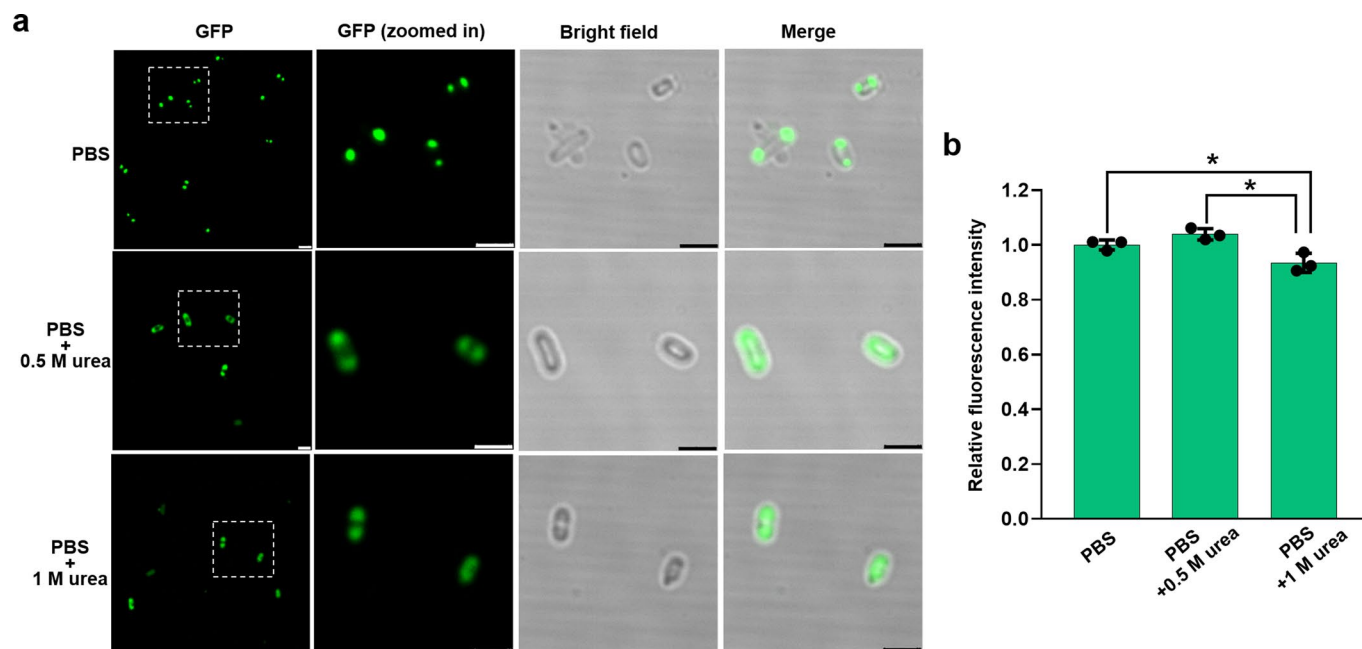
Extended Data Fig. 3 | Characterization of the dynamic compartments within *E. coli* cells by urea perturbation. a, Images of the I16-GFP expressing cells upon treatment with varying levels of urea. The recombinant *E. coli* cells were induced with 200 µM IPTG at 30 °C for 6 h, harvested, and resuspended in PBS buffer without and with the addition of urea. Following incubation at 25 °C for 20 min, the cells were imaged. Scale bars, 2.5 µm. **b**, Relative fluorescence of the cells upon treatment with varying levels of urea. Data are presented as mean ± s.d. of *n* = 3 biologically independent samples, with individual data points shown as black dots. The asterisks represent statistical significance with *P*-value < 0.05 based on one-way analysis of variance (ANOVA). Data in **a**, **b** are representative of *n* = 3 independent experiments. Note that the data reveals disassembly of the I16-GFP condensates for the urea-treated cells in a dose-dependent manner, with the cell morphology and fluorescence well retained. These results indicate that the molecular interactions of forming spidroin condensates are relatively weak and easy to be broken with the hydrogen bonding disruptor (urea), thus offering a new line of evidence proving the condensates are liquid-like.
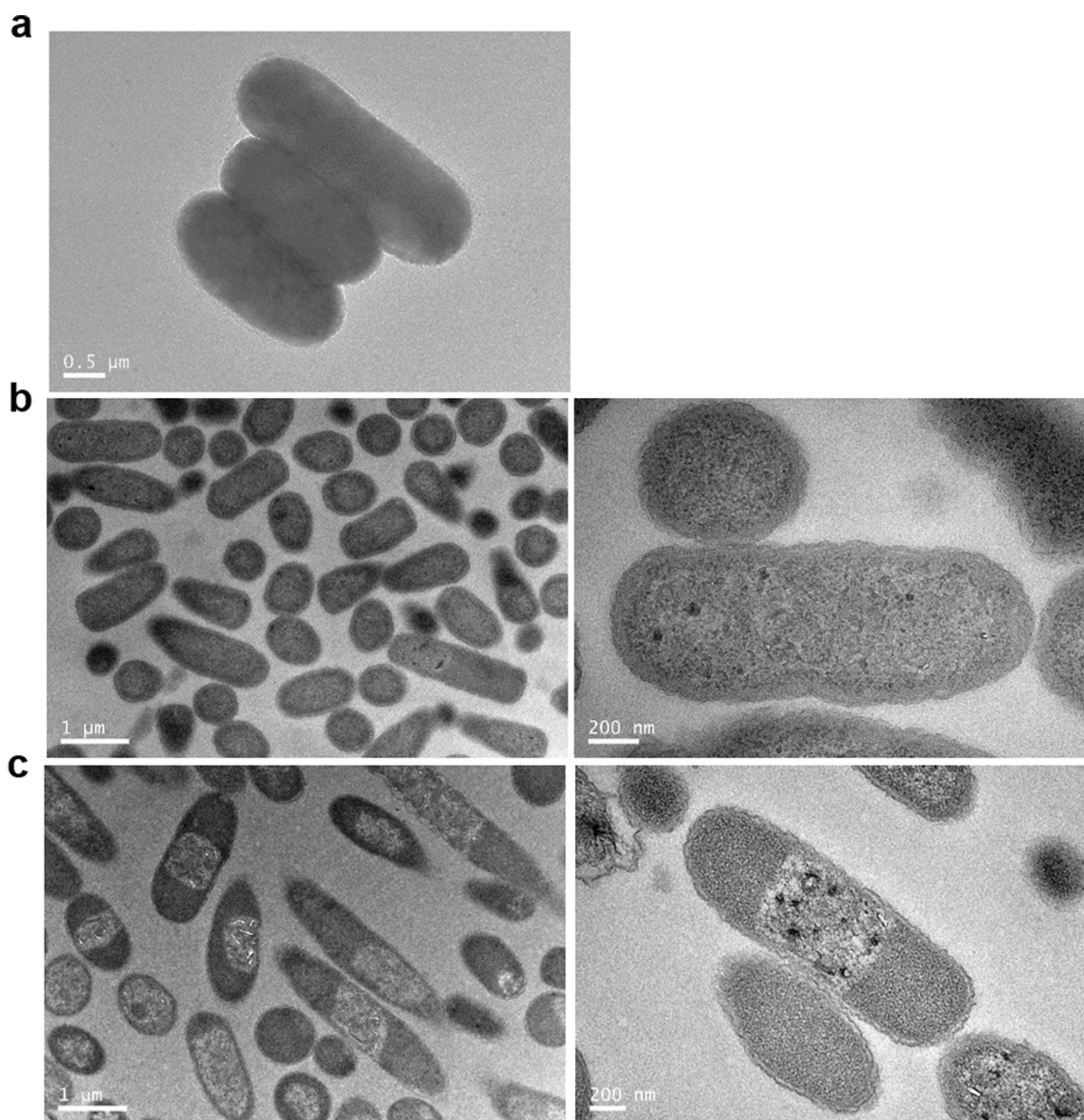
Extended Data Fig. 4 | TEM analyses revealed the formation of silk-based compartments in the cytoplasm. a, TEM image of fixed control cells without silk I16 expression. TEM images of microtome slices of *E. coli* cells without (**b**) and with expression of silk I16 protein (**c**). The cell samples were taken at 6 h after exposure to the inducer IPTG for silk gene expression at 37 °C. Note that clear compartmentalization was observed in the silk-expressing cells, but not in the control, non-expressing cells. Data in **a–c** are representative of *n* = 3 independent experiments.
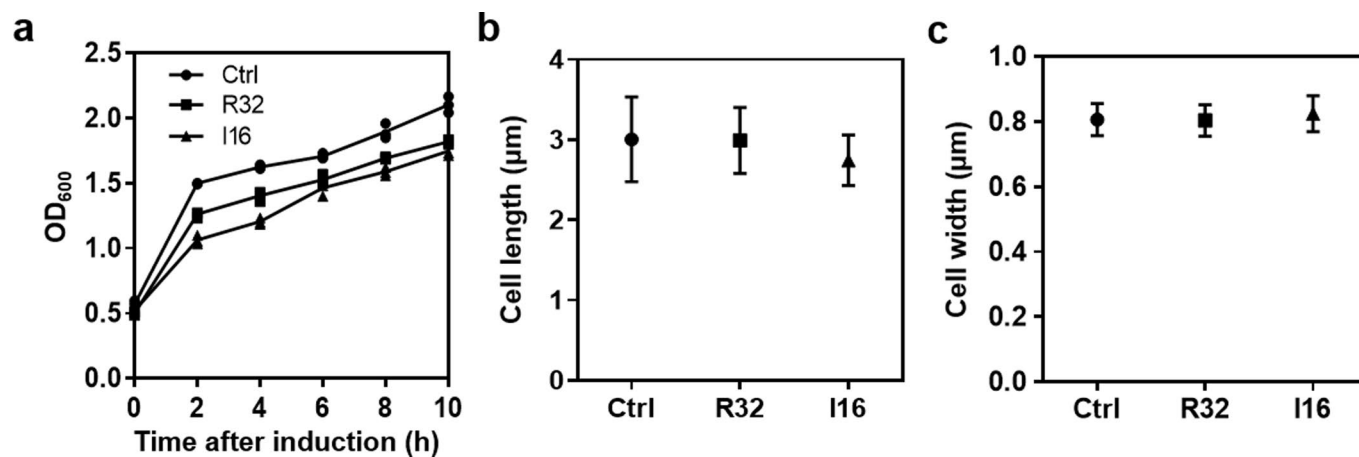
Extended Data Fig. 5 | Effects of formation of compartments on the cell growth and morphology. The growth (**a**), length (**b**), and width (**c**) of *E. coli* cells expressing recombinant major ampullate spidroin 1 (I16) and resilin-like protein (R32), and the control cells harboring empty vector. All cells were induced with 200 μM IPTG at 30 °C, and cell OD_{600} measured at the indicated time after induction. For evaluation of cell size, the cell samples were taken at 6 h post-induction for bright field light microscopy analyses. The data in **a** are presented as mean ± s.d. of $n = 3$ biologically independent samples, with individual data points shown. The data in **b** and **c** represent the average of 20 cells and error bars correspond to the standard deviations. Statistical significance was determined using one-way ANOVA for *P* values. Note that neither the cell length nor width was significantly altered upon protein production. Data in **a-c** are representative of $n = 2$ independent experiments.
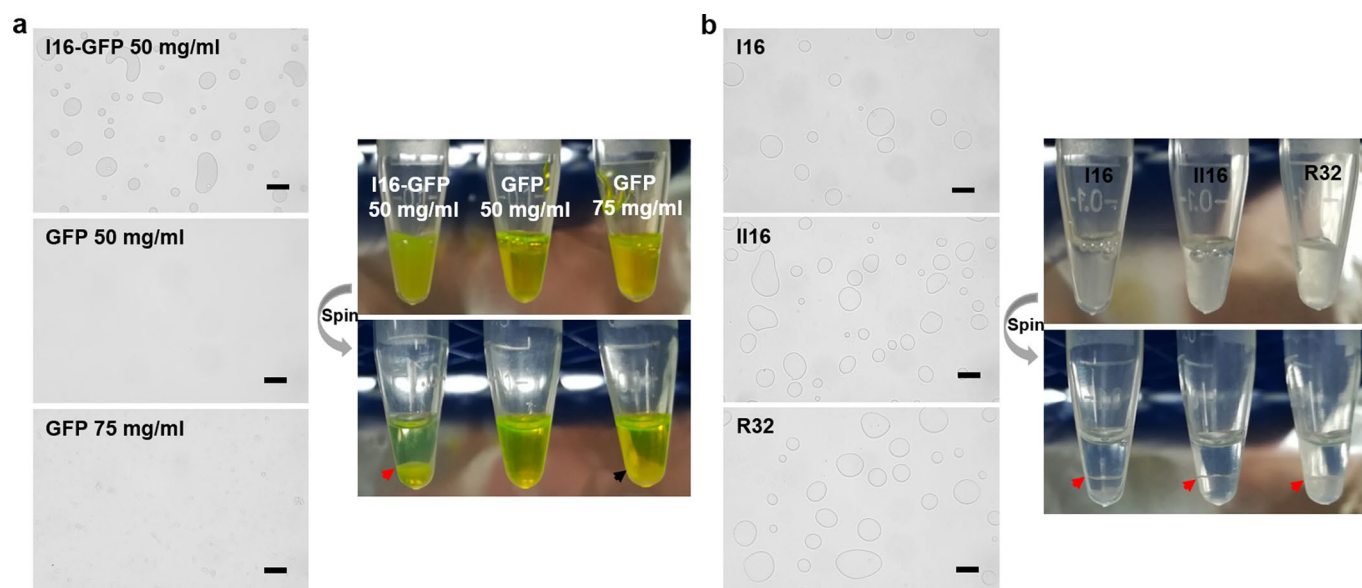
Extended Data Fig. 6 | *In vitro* reconstitution of the purified proteins with macromolecular crowder dextran-70. a, Reconstituted mixtures containing 50 mg/ml dextran-70 and I16-GFP were visualized by bright-field light microscopy, and spun by centrifugation to show separation into two liquid phases. Included as controls were reconstituted GFP at a final concentration of 50 mg/ml (no phase separation) or 75 mg/ml (aggregation). The red arrow indicates the coexistence of two liquid phases, whereas the black indicates the coexistence of a liquid phase and a solid phase of GFP aggregates. **b**, Reconstituted mixtures containing dextran-70 and each of the indicated proteins at 50 mg/ml were visualized by light microscopy, and spun by centrifugation to show separation into two liquid phases. Scale bars in **a**, **b**, 100 μm. Data in **a**, **b** are representative of *n* = 2 independent experiments.
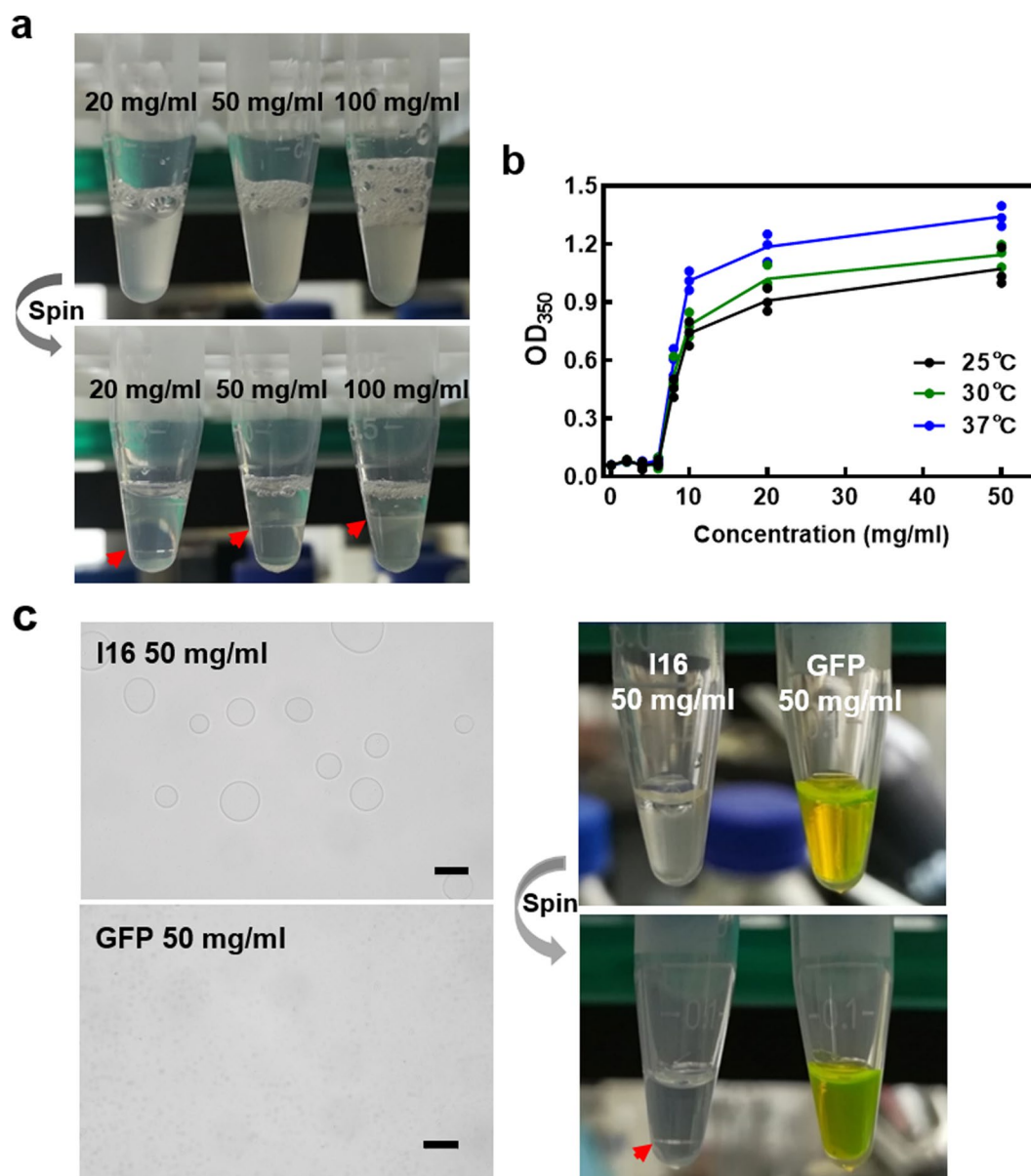
**Extended Data Fig. 7 | Liquid-liquid phase separation (LLPS) of the spider silk I16 protein *in vitro*. a**, Reconstitution of the purified I16 protein at varying final concentrations with the macromolecular crowding agent, dextran-70 at room temperature. The turbid mixtures were spun by centrifugation to show the co-existence of two liquid phases, as indicated by the red arrows in the photograph. **b**, Turbidity profiles of silk I16 as a function of protein concentration in the reconstituted mixtures at diverse temperatures. Data are presented as mean ± s.d. of $n = 3$ biologically independent samples, with individual data points also shown. Note that LLPS of I16 occurred at concentrations beyond critical values of approximately 6 mg/ml. **c**, Reconstituted mixtures containing I16 and macromolecular crowder Ficoll 70 were visualized by light microscopy, and spun to show separation into two liquid phases. Recombinant GFP was also included as a control. Scale bars in **c**, 100 µm. Data in **a**–**c** are representative of $n = 2$ independent experiments.
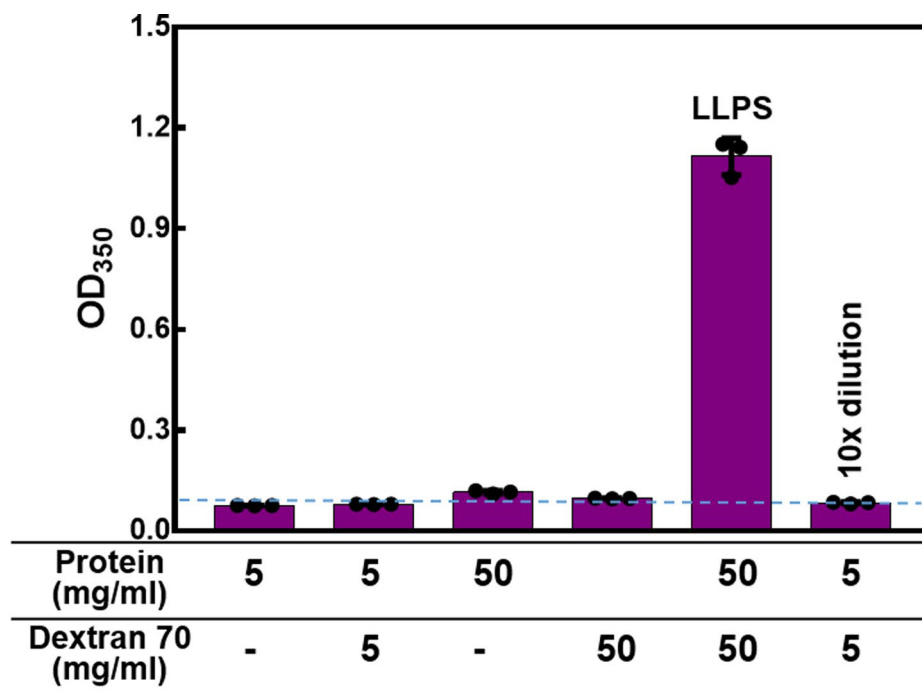
Extended Data Fig. 8 | Reversible liquid-liquid phase separation (LLPS) of the spider silk I16 protein upon dilution *in vitro*. Turbidity of the reconstituted mixtures with I16 and dextran 70 at the indicated concentrations was monitored by measuring optical density at 350 nm (OD_{350}). Data are presented as mean ± s.d. of $n = 3$ biologically independent samples (individual data points also shown), and are representative of $n = 2$ independent experiments.
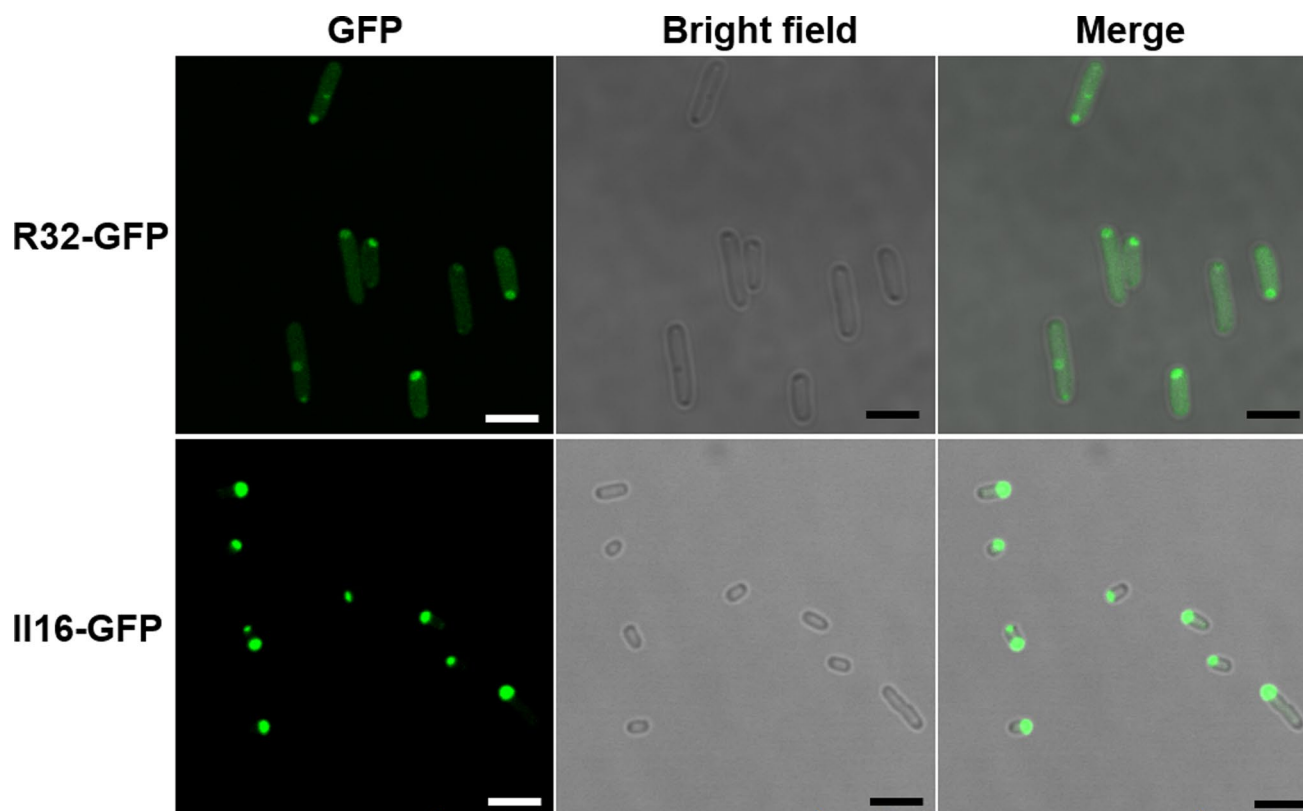
Extended Data Fig. 9 | Formation of cellular compartments in *E. coli* cells expressing recombinant resilin-like protein (R32) and major ampullate spidroin 2 (Il16). To visualize expression, both R32 and Il16 were fused N-terminally to GFP. *E. coli* cells harboring the corresponding plasmid constructs were induced with 200 μM IPTG at 30 °C, and cell samples were taken at 6 h post-induction for fluorescence and bright field microscopy analyses. Scale bars, 5 μm. Data are representative of *n* = 3 independent experiments.
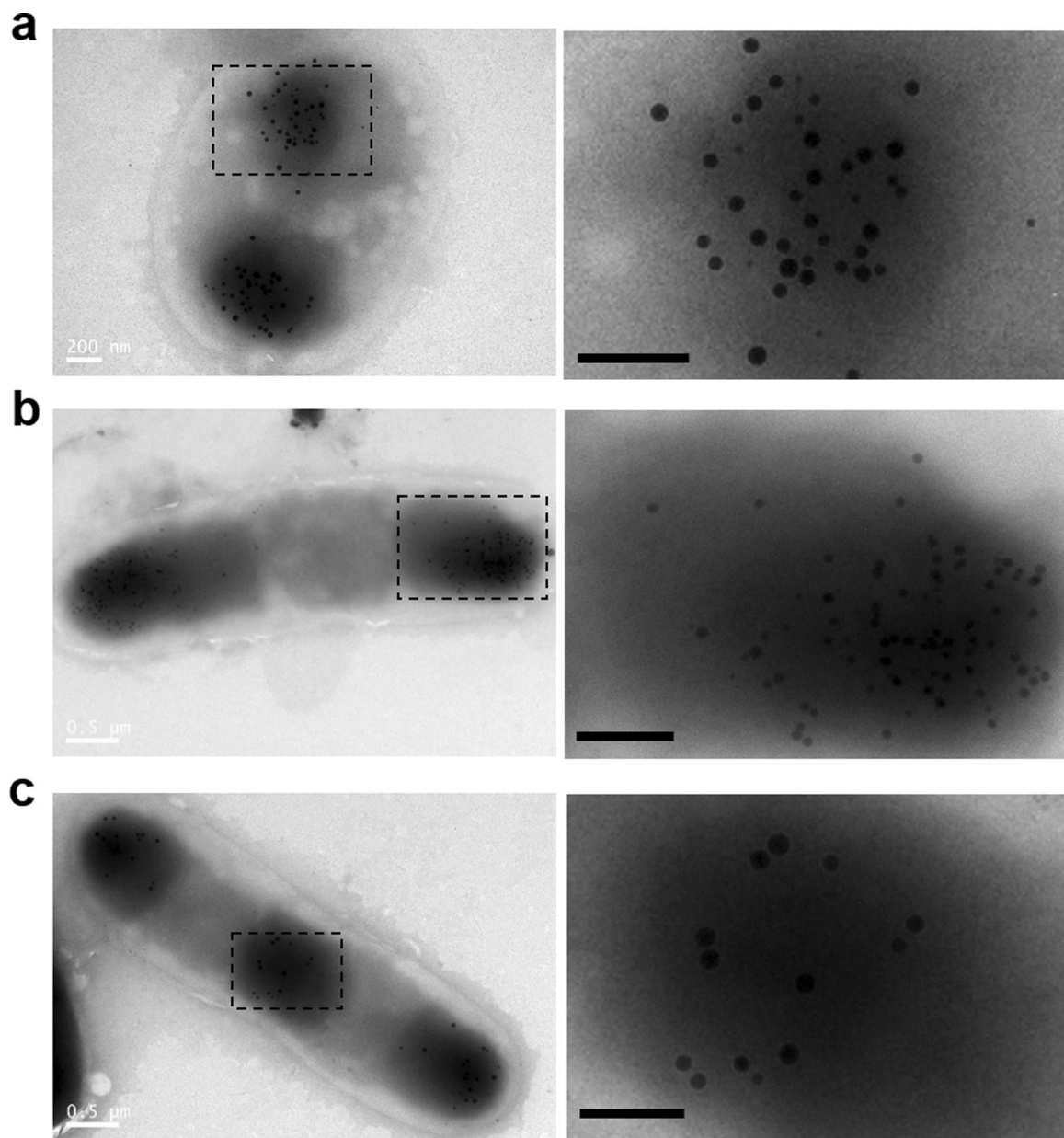
Extended Data Fig. 10 | Functional membraneless compartments for bioproduction of nanoparticles (NPs) within *E. coli* cells. a, **b**, and **c**, TEM images of individual cells expressing I16-MT for the production of Se NPs (left panel). The dotted boxes (left panels) are shown at a higher magnification at the right (scale bars, 200 nm). Data in **a**–**c** are representative of $n = 3$ independent experiments.

Corresponding author(s): Xiao-Xia Xia

Last updated by author(s): Apr 13, 2020

Reporting Summary

Nature Research wishes to improve the reproducibility of the work that we publish. This form provides structure for consistency and transparency in reporting. For further information on Nature Research policies, see Authors & Referees and the Editorial Policy Checklist.

Statistics

For all statistical analyses, confirm that the following items are present in the figure legend, table legend, main text, or Methods section.

n/a	Confirmed	
☐	☒	The exact sample size (*n*) for each experimental group/condition, given as a discrete number and unit of measurement
☐	☒	A statement on whether measurements were taken from distinct samples or whether the same sample was measured repeatedly
☐	☒	The statistical test(s) used AND whether they are one- or two-sided *Only common tests should be described solely by name; describe more complex techniques in the Methods section.*
☒	☐	A description of all covariates tested
☒	☐	A description of any assumptions or corrections, such as tests of normality and adjustment for multiple comparisons
☐	☒	A full description of the statistical parameters including central tendency (e.g. means) or other basic estimates (e.g. regression coefficient) AND variation (e.g. standard deviation) or associated estimates of uncertainty (e.g. confidence intervals)
☒	☐	For null hypothesis testing, the test statistic (e.g. *F*, *t*, *r*) with confidence intervals, effect sizes, degrees of freedom and *P* value noted *Give P values as exact values whenever suitable.*
☒	☐	For Bayesian analysis, information on the choice of priors and Markov chain Monte Carlo settings
☒	☐	For hierarchical and complex designs, identification of the appropriate level for tests and full reporting of outcomes
☒	☐	Estimates of effect sizes (e.g. Cohen's *d*, Pearson's *r*), indicating how they were calculated

Our web collection on statistics for biologists contains articles on many of the points above.

Software and code

Policy information about availability of computer code

Data collection	SDS-PAGE: Microtek Bio-5000 Plus scanner Confocal imaging and FRAP: Leica TCS SP8 STED 3X microscope Fluorescence measurements: Spark multimode microplate reader TEM: Tecnai G2 Spirit BioTWIN transmission electron microscope DLS: NanoBrook Omni system HPLC: Agilent 1200 HPLC system
Data analysis	GraphPad Prism 7.0 for graph plotting Microsoft Excel 2016 for statistical analysis Leica Application Suite X (LAS X) for confocal image analysis Image J 1.52u for band intensity analysis Particle Solutions Software (V 3.1) for DLS data analysis

For manuscripts utilizing custom algorithms or software that are central to the research but not yet described in published literature, software must be made available to editors/reviewers. We strongly encourage code deposition in a community repository (e.g. GitHub). See the Nature Research guidelines for submitting code & software for further information.

Data

Policy information about availability of data

All manuscripts must include a data availability statement. This statement should provide the following information, where applicable:

- Accession codes, unique identifiers, or web links for publicly available datasets
- A list of figures that have associated raw data
- A description of any restrictions on data availability

The data that support the findings of this study are available from the corresponding author on reasonable request

Field-specific reporting

Please select the one below that is the best fit for your research. If you are not sure, read the appropriate sections before making your selection.

☒ Life sciences   ☐ Behavioural & social sciences   ☐ Ecological, evolutionary & environmental sciences

For a reference copy of the document with all sections, see nature.com/documents/nr-reporting-summary-flat.pdf

Life sciences study design

All studies must disclose on these points even when the disclosure is negative.

Sample size	Sample sizes were not predetermined. We generally used sample sizes of 3 biological replicates, which can provide necessary statistical support. For cell length and width analysis (Extended data Fig.5) , 20 cells were tested and analyzed.
Data exclusions	Data were not excluded from analysis.
Replication	All biological experiments were successfully reproduced in independent experiments.
Randomization	The clones were picked up randomly during the experiments. To compare the effects of different treatments in a single experiment, the cells were from the same overnight culture.
Blinding	No blinding was conducted, because blinding would not provide any reliable datasets for our all biochemical and genetic experiments.

Reporting for specific materials, systems and methods

We require information from authors about some types of materials, experimental systems and methods used in many studies. Here, indicate whether each material, system or method listed is relevant to your study. If you are not sure if a list item applies to your research, read the appropriate section before selecting a response.

Materials & experimental systems

n/a	Involved in the study
☒	☐ Antibodies
☒	☐ Eukaryotic cell lines
☒	☐ Palaeontology
☒	☐ Animals and other organisms
☒	☐ Human research participants
☒	☐ Clinical data

Methods

n/a	Involved in the study
☒	☐ ChIP-seq
☒	☐ Flow cytometry
☒	☐ MRI-based neuroimaging